



## Multifunctional carbon-armored Ni electrocatalyst for hydrogen evolution under high current density in alkaline electrolyte solution

Yang Tang <sup>a</sup>, Fan Liu <sup>a</sup>, Wenqian Liu <sup>a</sup>, Shaoli Mo <sup>a</sup>, Xiaohong Li <sup>b</sup>, Daxiang Yang <sup>c</sup>, Yijun Liu <sup>a,\*</sup>, Shu-Juan Bao <sup>a,\*</sup>

<sup>a</sup> Key Laboratory of Luminescence Analysis and Molecular Sensing, Ministry of Education, School of Materials and Energy, Southwest University, Chongqing 400715, PR China

<sup>b</sup> Renewable Energy Group, College of Engineering, Mathematics and Physical Sciences, University of Exeter, Penryn Campus, Cornwall TR10 9FE, UK

<sup>c</sup> Chongqing Key Laboratory of Green Aviation Energy and Power, The Green Aerotechnics Research Institute of Chongqing Jiaotong University, Chongqing 401135, PR China



### ARTICLE INFO

#### Keywords:

Hydrogen Evolution Reaction  
Multifunctional carbon  
Electrocatalyst  
Superhydrophilic  
Ultrahigh-current density

### ABSTRACT

Hydrogen evolution reaction (HER) electrocatalysts capable of long-term operation under high current densities are key to the industrialization of water-splitting technology. Although numerous efforts have been devoted to expose active sites sufficiently while increasing the intrinsic catalytic activity, effects of non-kinetic factors on catalytic efficiency have not yet been comprehensively investigated. Herein, multifunctional carbon-armored nickel nanoparticles (NC@NiNPs) were fabricated using an in-situ polymer encapsulation method for use as a HER electocatalyst. NC@NiNPs exhibited low overpotential (74 mV at 10 mA cm<sup>-2</sup>), low Tafel slope (85.49 mV dec<sup>-1</sup>) and excellent stability (over 260 h at 1400 mA cm<sup>-2</sup>). Surprisingly, although the intrinsic activity of NC@NiNPs was lower than that of commercial 20 % Pt/C, NC@NiNPs provided markedly greater current density than 20 % Pt/C as the operating voltage was increased. This result implied that non-kinetic factors influenced the HER process, prompting this investigation to identify these unknown factors.

### 1. Introduction

Massive energy consumption based on use of traditional fossil fuels has triggered numerous environmental issues, prompting researchers to urgently explore cost effective and environmentally friendly renewable energy sources toward achieving global carbon neutrality [1–3]. In recent years, green hydrogen has attracted much attention as an energy carrier, due to its high thermal combustion value and zero-carbon emission [4,5], with electrolysis viewed as a promising option for carbon-free hydrogen production. However, due to a lack of highly efficient catalysts, this process requires high energy consumption to drive the hydrogen evolution reaction (HER), which is thermodynamically nonspontaneous [6,7]. Currently, commercial water electrolysis is mainly catalyzed by platinum (Pt)-based catalysts that are scarce and costly, thus greatly limiting its large-scale applications [8,9]. Therefore, cheaper and more efficient electrocatalysts are required before electrolysis of water can be performed to generate hydrogen on an industrial scale [10].

In past decades, various transition metals, metal sulfides, phosphides, nitrides, selenides, and related derivatives have been widely studied, resulting in development of electrocatalysts that are less costly than Pt [11–13]. However, as compared with Pt-based catalysts, the performance of less costly catalysts has been far from satisfactory, especially at high-current densities needed to meet industrial demand [14]. In order to improve performance capabilities of these catalysts, various carbon-based supports with high surface areas, good conductivities, and chemical stabilities have been evaluated. Such materials have been demonstrated to reduce activation energies and accelerate catalytic reaction rates, leading to development of numerous carbon-supported catalyst designs and fabrication processes [15]. Recent catalyst designs have incorporated carbon-based materials that support maximal catalytic activity of immobilized catalysts [16,17]. In fact, some catalysts deliver surprisingly excellent performance that appears to be derived from synergistic interactions occurring between carbon supports and catalytically active centers [18,19]. Nevertheless, as is true for carbon-supported Pt catalysts, these catalytically active materials

\* Corresponding authors at: Key Laboratory of Luminescence Analysis and Molecular Sensing, Ministry of Education, School of Materials and Energy, Southwest University, Chongqing 400715, PR China

E-mail addresses: [liuj26@swu.edu.cn](mailto:liuj26@swu.edu.cn) (Y. Liu), [baoshj@swu.edu.cn](mailto:baoshj@swu.edu.cn) (S.-J. Bao).

still suffer from particle coalescence, Ostwald ripening, and catalyst detachment from carbon supports after numerous cycles of operation [20,21]. In addition, during large-scale industrial production, mechanical shock effects caused by generation of large numbers of H<sub>2</sub> gas bubbles can seriously damage catalyst supports, leading to catalyst-support detachment that further reduces catalytic performance [22,23].

As reported by the water electrolysis industry, working current densities of proton exchange membrane water electrolyzers (PEMWs) generally exceed 1.6 A cm<sup>-2</sup>, while current densities of alkaline water electrolyzers (AWES) have not yet reached the required minimum current density of 0.5 A cm<sup>-2</sup> [24]. Nonetheless, maintaining continuous operation of electrolyzers over long periods of time (>100,000 h) under such high working current densities is a daunting challenge that must be overcome with improved HER catalyst designs [25]. Against the backdrop of industrial applicability, achieving higher current densities at lower overpotential values and overcoming mechanical shock-induced catalyst damage are two key points that must be considered while developing new HER catalysts.

To resolve the abovementioned issues, researchers have strived to increase intrinsic activities of catalysts while focusing on developing methods that expose as many active sites as possible. However, non-kinetic factors that may severely influence HER catalyst performance have not yet been thoroughly investigated [26]. Herein, Ni, a catalyst used successfully in the alkaline electrolyzed water industry [27], was selected and evaluated for gas bubble effects on HER performance. Several layers of nitrogen-doped, carbon-coated Ni nanoparticles (NC@NiNPs) were prepared using a facile bottom-up, in-situ polymer encapsulation method. Armed with a uniquely thin carbon protective layer, NC@NiNPs of around 8 nm in diameter with Ni content as high as 89.4 % were generated in the absence of appreciable agglomeration. Moreover, the nanoparticles exhibited surprisingly high HER catalytic activity and stability, while also providing hydrogen evolution overpotential that approximated that obtained with 20 % Pt/C. More importantly, although the intrinsic activity of NC@NiNPs was lower than that of commercial 20 % Pt/C, the current density provided by NC@NiNPs far exceeded that of 20 % Pt/C as the operating voltage was increased. In addition, NC@NiNPs catalytic performance remained stable even after operation for over 260 h in 1 M KOH at 1400 mA cm<sup>-2</sup>, a current density that far exceeded the current density of 10 mA cm<sup>-2</sup> used for durability testing of most HER catalysts in previously reported studies [28]. Taken together, these experimental results suggest that excellent electrocatalytic activity and superior stability of NC@NiNPs may be attributed to the following factors: small nanoparticle size and high Ni content that ensure high current output [29,30]; nitrogen-doped carbon layer effects on the Ni electronic structure that promote rapid charge transfer among composite materials during HER cycles; effective carbon shield layer-based protection of the electrocatalyst from particle coalescence, Ostwald ripening, and electrochemical corrosion; and excellent hydrophilicity of the nitrogen-doped carbon layer that allows NC@NiNPs to rapidly divert adhered H<sub>2</sub> bubbles away from the catalyst to greatly decrease mechanical shock during long HER cycles (a requirement for industrial applicability) [31,32]. Overall, the results of this work indicate that the non-kinetic factor, H<sub>2</sub> gas bubble evolution, greatly influences HER process performance. Furthermore, our results suggest that our proposed in-situ polymer bottom-up encapsulation method may be a feasible approach for preparing various carbon coated transition metal-based catalysts for use in industrial-scale high-efficiency hydrogen evolution-based applications.

## 2. Experimental section

### 2.1. Materials

Ni(NO<sub>3</sub>)<sub>2</sub>·6H<sub>2</sub>O, polyvinylpyrrolidone (PVP, (C<sub>6</sub>H<sub>9</sub>NO)<sub>n</sub> MW 40000), ethylene glycol (EG), and KOH were obtained from Aladdin Co.,

Ltd., China. All reagents were used without further purification.

### 2.2. Preparation of NC@NiNPs, C@NiNPs, and NiNPs

PVP (2 g) was dissolved in 25 mL of ethylene glycol with stirring at 100 °C and 2 g of Ni(NO<sub>3</sub>)<sub>2</sub>·6H<sub>2</sub>O was dissolved in 20 mL of ethylene glycol at room temperature. Next, the two solutions were mixed together with stirring at 175 °C for 30 min, resulting in generation of a light green-colored emulsion. The emulsion was then centrifuged at 5000 r/min, the pellet containing the precursor was washed with ethanol, then the resulting solid powder was dried at 60 °C for 12 h. Thereafter, the powder was transferred to a porcelain crucible and annealed at 500 °C in an argon atmosphere for 2 h then the final product was collected and designated NC@NiNPs. For comparison, an additional product was prepared under the same conditions but in the absence of PVP (designated C@NiNPs). In addition, a third sample, designated NiNPs, was prepared from commercial 30-nm-diameter nickel nanoparticles that were washed with acetone while undergoing ultrasonic treatment to remove organic pollutants. Finally, the particles were soaked in 1 M hydrochloric acid for 1 h to remove surface oxide followed by washing of the nickel nanoparticles with deionized water to obtain pure NiNPs.

### 2.3. Preparation of C@NiNPs-0, NC@NiNPs-1, and NC@NiNPs-2

C@NiNPs-0, NC@NiNPs-1, and NC@NiNPs-2 were prepared using similar methods to that used to prepare NC@NiNPs except that different mass ratios of PVP to Ni<sup>2+</sup> were used. More specifically, mass ratios of 0, 1, and 2 were used to prepare samples designated C@NiNPs-0, NC@NiNPs-1, and NC@NiNPs-2, respectively.

### 2.4. Preparation of electrodes

In order to prepare a working electrode to evaluate catalytic activity, first a 3-mm-diameter glassy carbon electrode (GCE) was polished with Al<sub>2</sub>O<sub>3</sub>, rinsed with deionized water, then dried with nitrogen. Next, the polished GCE was coated with active material (0.025 mg). Meanwhile, 5 mg of previously prepared catalyst was added into 1 mL of Nafion solution composed of deionized water, ethanol, and Nafion at a volume ratio of 1:1:0.05 then the mixture was ultrasonically mixed for 30 min to generate catalyst ink. Finally, the catalyst ink (5  $\mu$ L) was dropped onto the clean GCE surface and allowed to dry naturally.

### 2.5. Electrochemical measurements

All electrochemical measurements were performed using an electrochemical workstation (CHI 760E, Chenhua Instruments Inc.). A Hg/HgO electrode (1 M KOH) and carbon rod were used as reference electrode and counter electrode, respectively, with 1 M KOH serving as the electrolyte. Linear scan voltammograms (LSV) were recorded at 5 mV s<sup>-1</sup>. Long-term stability testing was performed via chronoamperometry conducted at 1.6 V and 25 °C. Electrochemical impedance spectroscopy (EIS) measurements were detected within a frequency range of 0.01 Hz to 100 kHz. The main arc in the EIS spectrum was matched using a simplified Randles equivalent circuit. The Randles circuit was composed of a resistance (Rs) in series with a parallel arrangement of a charge-transfer resistance (Rct) and a constant phase element (CPE), with fitting parameters appraised via the Levenberg-Marquardt minimization procedure. Cyclic voltammetry (CV) was applied to measure the electrochemical double-layer capacitance at nonfaradaic potentials in order to determine the catalytic electrochemical active surface area (ECSA). More specifically, the ECSA was measured via electrochemical double-layer capacitance (Cdl) to estimate the active sites of the electrocatalyst, and it was calculated by measuring the capacitive current density at different scan rates. Overpotential values were calculated according to the following equation: E (overpotential, V) = E (vs. Hg/HgO) + 0.098 + 0.0592 pH.

### 3. Results and discussion

#### 3.1. Structures and morphologies of catalysts

Fig. 1a outlines the preparation process of the in-situ bottom-up polymer encapsulation method used to synthesize NC@NiNPs. Briefly, ethylene glycol (EG) serving as both solvent and reducing agent, together with polyvinylpyrrolidone (PVP) to capture free  $\text{Ni}^{2+}$  through electrostatic action [33]. PVP reduced the surface energy, due to the ability of its flexible polymer chains to easily wrap around  $\text{Ni}^{2+}$  ions to form polymer-coated Ni-containing spheres. During reduction and calcination processes, long PVP chains act to maintain steric hindrance between nickel ions and prevent Ni nanoparticle agglomeration by forming a thin carbon layer that coats Ni particle surfaces [34]. Next, thermogravimetric analysis was conducted that demonstrated that optimal pyrolysis occurred at 500 °C (more detailed procedures are shown in the experimental section). Thus, this temperature was used for conducting pyrolysis thereafter (Fig. S1), with microstructural and phase characterization results of precursors shown in Fig. S2.

Meanwhile, NiNPs and C@NiNPs were also synthesized for use as comparison samples (please refer to the Experimental Section for details). As displayed in Fig. 1b, three peaks in the XRD pattern at 20 of 44°, 52°, and 76° are visible that correspond to standard  $d_{hkl}$  patterns of (111), (200), and (220), respectively, for metallic nickel (PDF standard card #04-0850). The broad diffraction peak around 25° corresponds to the (002) plane of graphitic carbon [35]. Respective D and G bands observed at  $\sim 1300 \text{ cm}^{-1}$  and  $1600 \text{ cm}^{-1}$  within the Raman spectrum (Fig. 1c) confirmed successful formation of graphitic carbon from precursor materials [36]. In addition, transmission electron microscopy (TEM) image results showed morphologies and microstructures of particles within the final NC@NiNPs preparation (Fig. 1d), wherein nickel nanoparticles with an average diameter of 8 nm can be seen that are uniformly distributed across the field of view. Under high-resolution TEM, a well-defined lattice fringe of length 0.207 nm was observed that corresponds to the (111) crystal plane of Ni (Fig. 1e). These very tiny Ni particles were covered with several layers of carbon, a material known to influence Ni electronic structure, endow Ni ions with superior catalytic activity and act as battle armor to stabilize NiNPs during

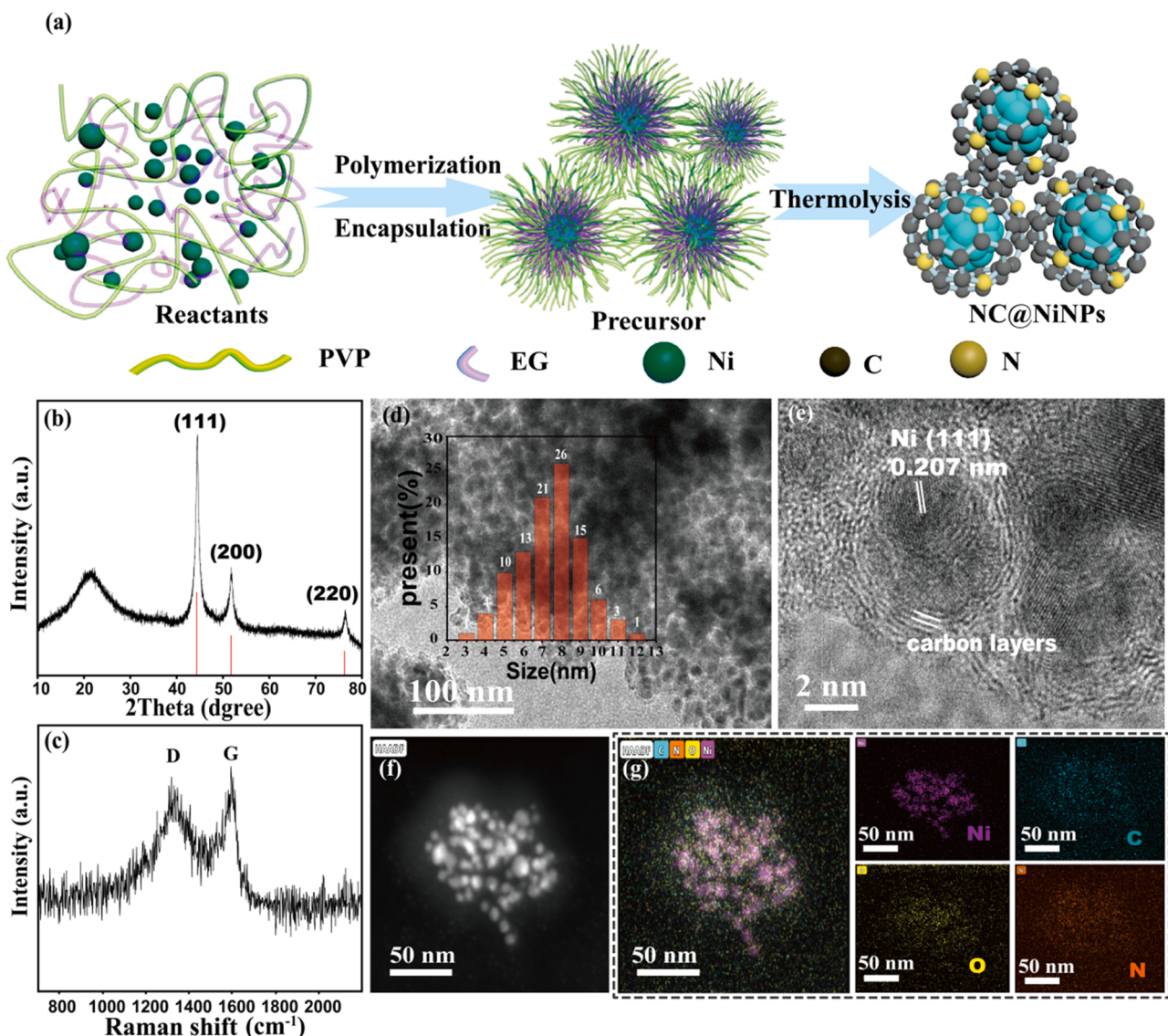
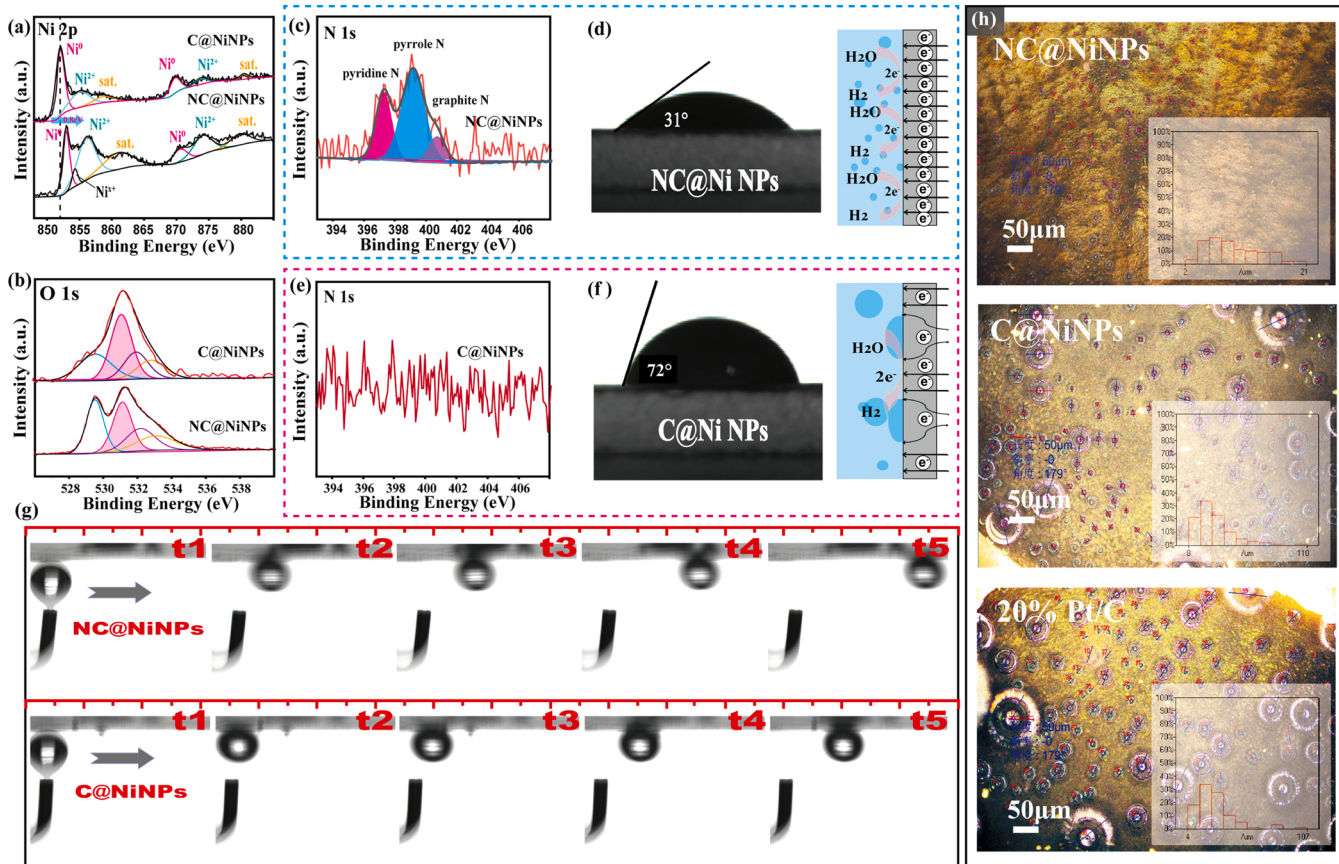


Fig. 1. (a) Schematic illustration showing the NC@NiNPs electrocatalyst synthesis method and microstructure. (b) X-ray diffraction (XRD) pattern of NC@NiNPs. (c) Raman spectrum of NC@NiNPs. (d and e) Transmission electron microscopy (TEM) images of NC@NiNPs at low and high magnifications, respectively, with insert in panel (d) showing particle size distribution. (f) High-angle annular dark-field scanning transmission electron microscopy (HAADF-STEM) and (g) energy dispersive spectroscopy (EDS) elemental mapping images of NC@NiNPs (with individual elements of Ni, C, O, and N shown in small four panels to the right).

multiple HER cycles. When considered together with field emission scanning electron microscopy (FESEM) results presented in Fig. S3, these results suggest that the carbon-coated Ni particles are connected to one another by a conductive carbon skeleton to form a 3D interconnected networked structure. Additionally, high-angle annular dark-field scanning transmission electron microscopy (HAADF-STEM) images and energy dispersive spectroscopy (EDS) elemental mapping results (Fig. 1f, Fig. 1g) confirmed that NC@NiNPs possessed predicted elemental composition characteristics and were uniformly distributed nanoparticles, while results of inductively coupled plasma (ICP analysis) (Table S1) indicated that Ni content in NC@NiNPs was 89.4<sub>WT</sub>%.

X-ray photoelectron spectrometry (XPS) was conducted to study elemental compositions and surface chemical states of NC@NiNPs and C@NiNPs, with the results shown in Fig. 2a, Fig. S4, and S5. Notably, a peak corresponding to Ni<sup>2+</sup> at ~855 eV was observed within the Ni 2p spectrum of NC@NiNPs, which is obviously stronger than the corresponding peak in the C@NiNP spectrum [37]. This result indicated that PVP ketone functional groups are capable of chelating Ni<sup>2+</sup> to support formation of a greater number of nickel-oxygen bonds in the NC@NiNPs precursor than are formed in the C@NiNPs precursor [38]. During subsequent pyrolysis reduction processes, most Ni within NiO was converted to Ni during the generation of numerous oxygen vacancies [39]. Further comparisons of XPS spectra between NC@NiNPs and C@NiNPs revealed a positive shift in the position of the peak corresponding to Ni<sup>0</sup> in NC@NiNPs of 0.8 eV, which may have resulted from both the removal of oxygen from the partial lattice and from electro-negative nitrogen-associated interference with nickel electronic structure [40]. Interestingly, a small peak between Ni<sup>0</sup> and Ni<sup>2+</sup> was

observed in the Ni 2p spectrum of NC@NiNPs that indicated that more oxygen vacancies existed in NC@NiNPs than in C@NiNPs. In addition, the O1s spectra of both samples (Fig. 2b) contained peaks at ~532 eV and ~533 eV that were attributed to C=O and adsorbed oxygen, respectively, while the stronger peak appearing at 531.2 eV for both samples corresponded to the surface oxygen vacancy and the peak at 529.8 eV corresponded to lattice oxygen [41]. Obviously, more lattice oxygen was present in NC@NiNPs than in C@NiNPs, which is consistent with the abovementioned Ni 2p spectral results [42,43]. Meanwhile, N 1s spectra (Fig. 2c, Fig. 2e) clearly indicated that NC@NiNPs were successfully doped with nitrogen, while on the other hand, no peak was observed in the N 1s spectrum of C@NiNPs. Moreover, the three peaks shown in Fig. 2c at 397.5 eV, 399.5 eV, and 400.7 eV corresponded to peaks for pyridine N, pyrrole N and graphite N, respectively [44]. As shown in Fig. S6, a clear peak located at 286 eV could be assigned to a C-N bond as further evidence that successful doping of nitrogen with carbon occurred in NC@NiNPs. Notably, it is generally believed that nitrogen doping may activate adjacent carbon atoms to enhance H adsorption to surfaces of NC@NiNPs [32]. In order to better understand the hydrophilicity of catalyst materials, contact angle measurements were conducted on NC@NiNPs (Fig. 2d) and C@NiNPs (Fig. 2f), with results and schematics of bubble evolution behavior on corresponding electrodes presented in Fig. 2d and Fig. 2f, respectively. Interestingly, it was found that NC@NiNPs exhibited a contact angle of 31°, which is much smaller than that observed for C@NiNPs (72°). This result suggests that NC@NiNPs nanoparticles possess better hydrophilic properties and thus enable faster H<sub>2</sub> bubble ejection as compared to C@NiNPs. Furthermore, this result is in good agreement with zeta potential



**Fig. 2.** High-resolution X-ray photoelectron spectrometry (XPS) spectra of NC@NiNPs and C@NiNPs. (a) Ni 2p spectra for NC@NiNPs and C@NiNPs. (b) O 1s spectra for NC@NiNPs and C@NiNPs. (c) N 1s spectrum for NC@NiNPs. (d) Contact angle and electrochemical processes that occur within gas-evolving electrodes of NC@NiNPs. (e) N 1s spectrum for C@NiNPs. (f) Contact angle and electrochemical processes within gas-evolving electrodes of C@NiNPs. (g) Comparisons of surface bubble evolution velocities between NC@NiNPs and C@NiNPs. (h) Digital photos of H<sub>2</sub> bubble evolution on NC@NiNPs, C@NiNPs and 20 % Pt/C respectively (insert: statistics of bubble size distribution).

measurement results (Fig. S7), which revealed that the zeta potential of C@NiNPs was close to zero ( $-2$  mV), while that of NC@NiNPs was  $-24$  mV. The more negative zeta potential of NC@NiNPs indicated that the more nucleophilic the samples became due to their lone pairs of N2p<sub>z</sub> electrons in NC@NiNPs [45]. Such superior hydrophilicity of NC@NiNPs would also facilitate rapid displacement of gas bubbles away from the catalyst surface. To further confirm this point, *in situ* experiments were carried out to monitor transient migratory behavior of gas bubbles as they formed and moved across surfaces of NC@NiNPs and C@NiNPs (Fig. 2 g). Ultimately, these results revealed that gas bubbles moved markedly faster across NC@NiNPs surfaces than across C@NiNPs surfaces, with additional details presented in Supplementary Movie S1. In addition, nucleation and growth of H<sub>2</sub> bubbles on different electrodes were observed using an optical microscope. As shown in Fig. 2h, diameters of bubbles formed on surfaces of the NC@NiNPs electrode were mainly distributed within the range of 2–21  $\mu$ m, which were significantly smaller than diameters of bubbles that formed on electrode surfaces of C@NiNPs (8–110  $\mu$ m) and 20 % Pt/C (4–102  $\mu$ m). These results indicated that the lower limit of H<sub>2</sub> bubble size on NC@NiNPs was far smaller than corresponding lower limits for the other electrocatalysts. In turn, a lower bubble size limit may have greatly shortened the residence times of bubbles at the reaction interface to greatly reduce the bubble shielding effect and thereby improve hydrogen production efficiency [46].

Supplementary material related to this article can be found online at doi:10.1016/j.apcatb.2022.122081.

### 3.2. HER performance of NC@NiNPs

After performance tests of NiNPs, C@NiNPs, and NC@NiNPs were conducted under identical conditions, the results were compared to those obtained for 20 % Pt/C catalyst and expressed as linear sweep voltammetry (LSV) curves (without iR correction) [47] (Fig. 3a). The results indicate that although 20 % Pt/C delivered a near-zero onset overpotential with increasing work voltage, the current density delivered by NC@NiNPs far exceeded that delivered by the 20 % Pt/C catalyst. In addition, NC@NiNPs exhibited excellent HER performance, with

an overpotential of only 74 mV observed at a current density of 10 mA cm<sup>-2</sup> that was far superior to that observed for NiNPs (307 mV) and C@NiNPs (174 mV), and only slightly higher than that observed for 20 % Pt/C (34.6 mV) (Fig. S8). Meanwhile, Tafel slopes determined for 20 % Pt/C and NC@NiNPs were 57.24 mV dec<sup>-1</sup> and 85.49 mV dec<sup>-1</sup>, respectively, (Fig. 3b), implying that HER process rates associated with these catalysts were controlled by the Volmer-Heyrovsky mechanism [48]. Importantly, these HER process rates are far lower than corresponding rates calculated for catalysts C@NiNPs (153.84 mV dec<sup>-1</sup>) and NiNPs (256 mV dec<sup>-1</sup>). Moreover, EIS spectra (Fig. S9) further confirmed the smaller charge transfer resistance and higher electrical conductivity of NC@NiNPs as compared to corresponding features of C@NiNPs and NiNPs under the same bias voltage [49]. Furthermore, the NC@NiNPs curve exhibited a parabolic shape that was slightly larger in area than that plotted for 20 % Pt/C, as is clearly shown in the Nyquist diagram in Fig. S9, thus demonstrating that a faster kinetic process was associated with 20 % Pt/C. However, the explanation underlying why the HER performance of NC@NiNPs under large current density was markedly superior to that of 20 % Pt/C still remains unclear, but we speculate that it may be attributed to non-kinetic factors, warranting further investigation. Additionally, the  $R_s$  value of NC@NiNPs was 7  $\Omega$ , which indicates that it possesses excellent electrical conductivity. As an additional consideration, electrochemical active surface area (ECSA) values for these electrocatalysts were estimated based on electrochemical double-layer capacitance ( $C_{dl}$ ) values (Fig. 3c, Fig. S10) [50], whereby the  $C_{dl}$  value of NC@NiNPs was 26.3 mF cm<sup>-2</sup>, a higher value than corresponding values calculated for C@NiNPs (9.1 mF cm<sup>-2</sup>) and NiNPs (4.3 mF cm<sup>-2</sup>). These results thus suggest that NC@NiNPs possessed the largest number of active sites. Finally, as shown in Fig. 3b, the electrocatalytic HER performance of NC@NiNPs prepared in alkaline media is almost optimal among non-noble metal nanocatalysts (as reported in the literature) and comparable to reported HER performance of platinum-based catalysts (Table S2).

Importantly, the HER stability of the NC@NiNPs-based electrode was evaluated by chronoamperometry analysis during exposure to a current density of 1400 mA cm<sup>-2</sup> (Fig. 4a). The results showed that even after 260 h of HER operation, output current density remained at

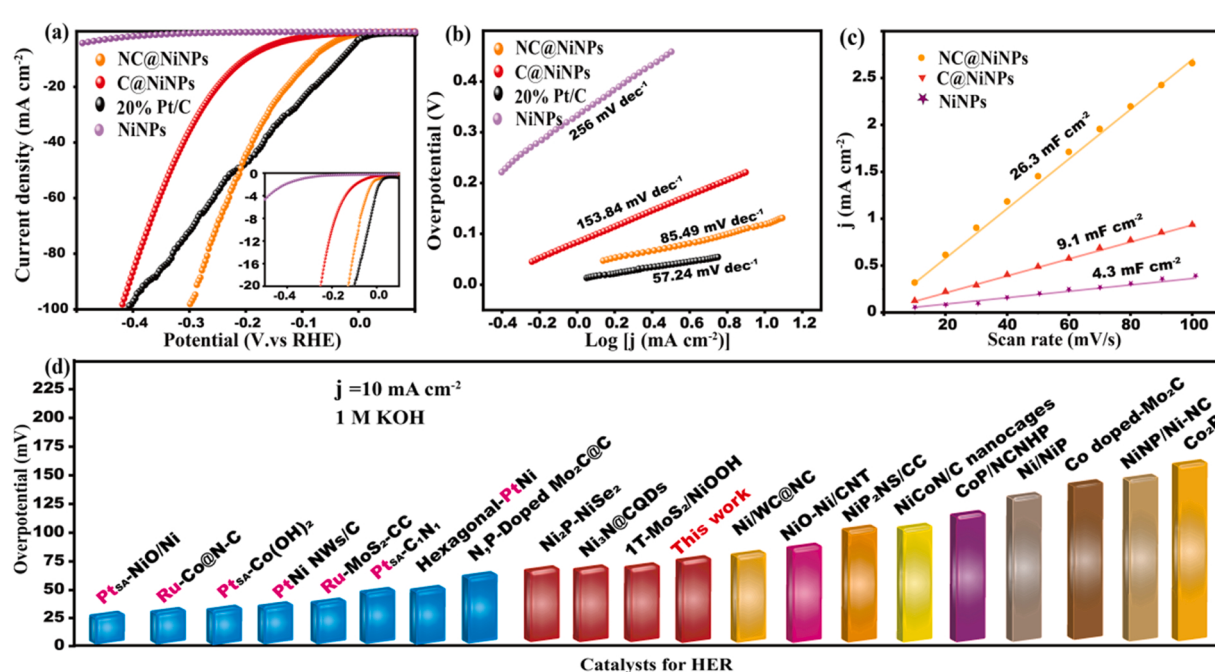
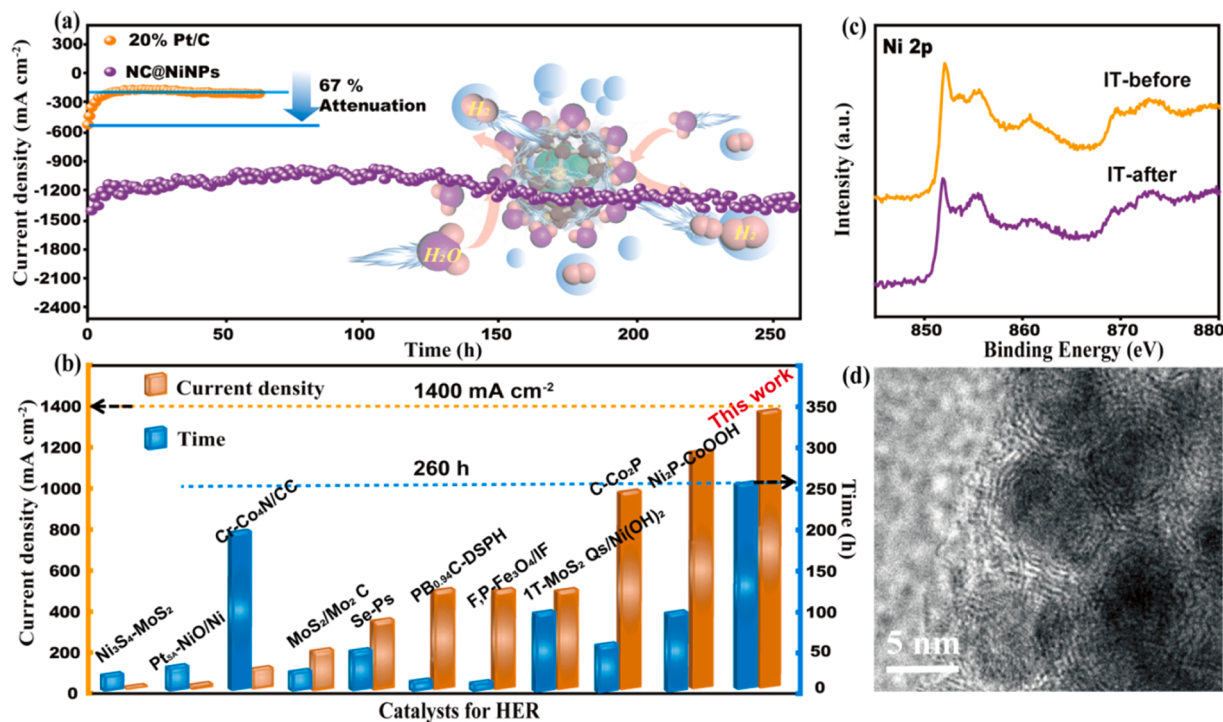


Fig. 3. (a) HER linear sweep voltammetry LSV curves of NiNPs, 20 % Pt/C, C@NiNPs, and NC@NiNPs. (b) Tafel plots of NiNPs, 20 % Pt/C, C@NiNPs, and NC@NiNPs. (c) Double-layer capacitance ( $C_{dl}$ ) values calculated from slopes of plotted current density values obtained for various scan rates for NC@NiNPs, C@NiNPs, and NiNPs. (d) Comparisons of HER activity of NC@NiNPs to HER activities of other reported catalysts, with HER activities presented in Table S2.



**Fig. 4.** (a) Chronoamperometry (at a static high current density of  $1400 \text{ mA cm}^{-2}$ ) of NC@NiNPs conducted after 260 h of HER operation, and commercial 20 % Pt/C conducted under the same conditions. (c) XPS spectra of NC@NiNPs before and after IT stability testing at  $1400 \text{ mA cm}^{-2}$ . (d) TEM images of NC@NiNPs after IT stability testing at  $1400 \text{ mA cm}^{-2}$ . (b) Comparisons of current density and stability values of NC@NiNPs to reported values for other catalysts. source data presented in Table S3.

$1400 \text{ mA cm}^{-2}$ , a performance level that was markedly superior to that observed for commercial 20 % Pt/C tested under the same conditions (Fig. 4a). To investigate why the NC@NiNPs electrode continued to work stably at such a high current density over such a long period of time, NC@NiNPs were analysed by XPS and TEM. As shown in Fig. 4c and Fig. 4d, the carbon armor was still clearly visible and intact, thus indicating the armor prevented both agglomeration of nano-Ni particles and Ni oxidation during numerous HER cycles. By contrast, NiNPs underwent severe oxidation after multiple reaction cycles (Fig. S11). Furthermore, the superior performance of this carbon armor was demonstrated by comparing intrinsic activities of NC@NiNPs obtained before and after long cycles (Fig. S12). As shown in Fig. 4b, our designed catalyst provided dramatically superior current density and long-cycle stability when operated in alkaline media as compared with corresponding previously reported performance indicators of cheap metal-based HER catalysts (Table S3).

### 3.3. Potential mechanism of NC@NiNPs formation

In order to investigate whether the presence of a carbon protective layer affected NC@NiNPs HER performance while optimizing the procedure for synthesizing this catalyst, NC@NiNPs were prepared under identical conditions except for addition of different quantities of PVP. From the results (Fig. 5a), it is obvious that PVP played an important role in carbon layer formation around nickel particles, whereby for a PVP to  $\text{Ni}^{2+}$  mass ratio of 0, obvious agglomeration of nickel nanoparticles occurred that prevented formation of a clear carbon layer. However, when the ratio was increased to 1 (Fig. 5b), a thin carbon protective layer was clearly visible that indicated the Ni nanoparticles were well protected and uniformly dispersed. Notably, when the procedure was scaled-up, high catalytic performance was maintained (Fig. S13). By contrast, when the ratio was further increased to 2 (Fig. 5c), an excessive amount of PVP was converted into a large quantity of carbon during pyrolysis that led to embedding of the metal active centers within the

carbon bulk phase. Regardless, XRD patterns of all of these samples (Fig. 5d) were all in agreement with the XRD pattern obtained for the Ni standard (PDF standard card # 04-0850). Nevertheless, as shown in Table S4, half-peak width values for these samples increased with increasing amount of converted PVP, which indicated that nanoparticle size decreased with increasing PVP conversion. To better understand the structure-activity relationships of these catalysts, their pore structures and specific surface areas were measured and are presented in Fig. S14b and S14c. The specific surface area of NC@NiNPs-1 was slightly smaller than that of NC@NiNPs-2, while NC@NiNPs-1 contained more abundant mesopores ( $\sim 20 \text{ nm}$ ) between particles (Fig. S14e) that may have facilitated entry of the electrolyte into the bulk phase. Furthermore, as shown in Fig. S14g, NC@NiNPs-1 possessed the largest gas bubble contact angle and the smallest water contact angle, which are closely related to the microstructure of pores and surface carbon layer. Unsurprisingly, even though the physical specific surface area of NC@NiNPs-1 was slightly smaller than surface areas of NC@NiNPs-2, the hierarchical pore distribution and excellent hydrophilicity of NC@NiNPs-1 still endowed them with the largest electrochemically active area (ECSA) (Fig. 5e, S15). In conclusion, these results indicate that controlling the thickness of the carbon layer and adjusting the pore structure are effective ways of maximizing catalytic activities of electrocatalysts. This point was further supported by results obtained from curves showing the relationship between overpotential and PVP dose (Fig. 5f), whereby when a ratio of PVP to  $\text{Ni}^{2+}$  of 1 was used to generate NC@NiNPs, the resulting nanocatalysts delivered the best HER performance. Taken together, the above-mentioned results were used to propose a potential mechanism of NC@NiNPs formation, which is presented in Fig. 5g.

### 4. Conclusion

In this work, multifunctional carbon armor-protected nano-Ni particles were prepared in a facile in-situ bottom-up encapsulation method. As compared with the commercial 20 % Pt/C HER electrocatalyst,

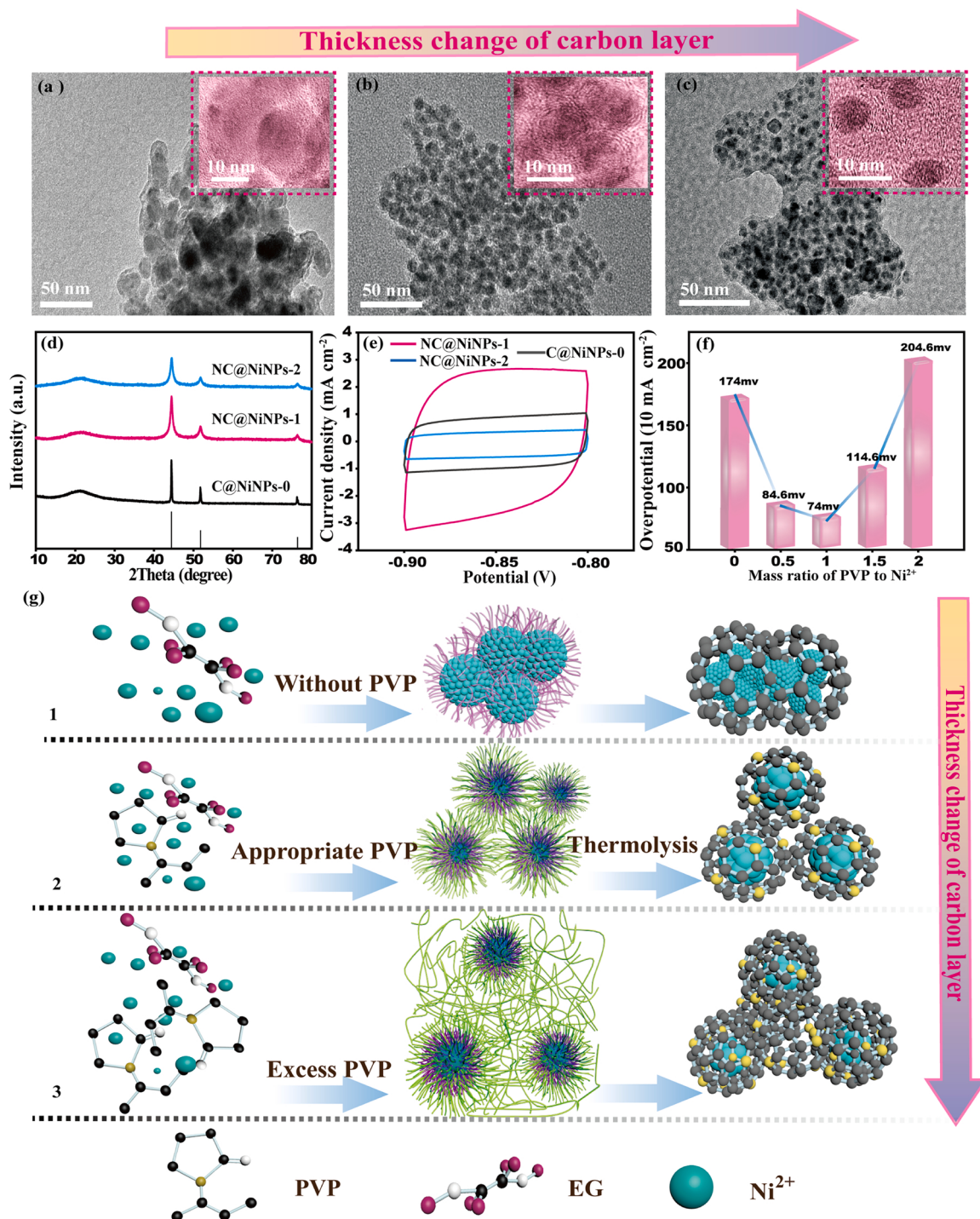


**Fig. 5.** TEM images of (a) C@NiNPs-0, (b) NC@NiNPs-1, (c) NC@NiNPs-2. (d) XRD patterns of C@NiNPs-0, NC@NiNPs-1, and NC@NiNPs-2. (e) CV curves generated using the same scan rates for C@NiNPs-0, NC@NiNPs-1, and NC@NiNPs-2. (f) Overpotential values at  $10 \text{ mA cm}^{-2}$  for different mass ratios of PVP to  $\text{Ni}^{2+}$ . (g) Schematic showing mechanism of NC@NiNPs formation for different PVP to  $\text{Ni}^{2+}$  mass ratios.

NC@NiNPs generated a much larger current density output and could operate stably for 260 h at  $1400 \text{ mA cm}^{-2}$  (overpotential = 674.6 mV) without degradation of catalytic performance, thus demonstrating that NC@NiNPs are far superior to 20 % Pt/C and most other reported non-precious metal catalysts. The excellent HER performance of NC@NiNPs was likely attributable to its multifunctional carbon layer, which improved NC@NiNPs performance via three mechanisms: by optimizing its electronic structure and increasing its electrochemical active area; by providing NC@NiNPs with a superhydrophilic surface that accelerated

charge transfer within the composite material that diverted attached  $\text{H}_2$  bubbles away from the catalyst surface; and by providing a protective carbon layer that prevented agglomeration of electrocatalyst particles, Ostwald ripening, and  $\text{H}_2$  bubble-induced mechanical shock during multiple HER cycles. Importantly, when the experiment was scaled up to assess its suitability for industrial-scale applications, the results demonstrated that the method is simple, easy to implement and highly repeatable. Thus, this method should be further developed as a prospective method for industrial-scale electrocatalyst production. Most

notably, the results of this work suggest that several non-kinetic factors, such as effects of interfacial hydrophobicity/hydrophilicity, ultra-high catalyst loading, and hierarchical porous structure, can greatly influence catalytic efficiencies of hydrogen evolution processes occurring at high current densities.

### CRediT authorship contribution statement

**Yang Tang:** Conceptualization, Methodology, Data curation, Writing – original draft preparation, Investigation. **Fan Liu:** Data curation, Formal analysis. **Wenqian Liu:** Visualization. **Shaoli Mo:** Software. **Xiaohong Li:** Writing – review & editing. **Daxiang Yang:** Funding acquisition. **Yijun Liu:** Supervision, Writing – review & editing. **Shu-Juan Bao:** Writing – review & editing, Project administration, Supervision.

### Declaration of Competing Interest

The authors declare that they have no known competing financial interests or personal relationships that could have appeared to influence the work reported in this paper.

### Data Availability

Data will be made available on request.

### Acknowledgements

This work is financially supported by the Chongqing Key Laboratory of Green Aviation energy and power, Chongqing, China (401135), National Natural Science Foundation of China (21972111, 22272131), Venture & Innovation Support Program for Chongqing Overseas Returnees (cx2019073), and Chongqing Engineering Research Center for Micro-Nano Biomedical Materials and Devices, and Chongqing Key Laboratory for Advanced Materials and Technologies, Chongqing Doctoral Research and Innovation Project (CYB21106).

### Appendix A. Supporting information

Supplementary data associated with this article can be found in the online version at [doi:10.1016/j.apcatb.2022.122081](https://doi.org/10.1016/j.apcatb.2022.122081).

### References

- [1] Z.W. Seh, J. Kibsgaard, C.F. Dickens, I. Chorkendorff, J.K. Nørskov, T.F. Jaramillo, Combining theory and experiment in electrocatalysis: insights into materials design, *Science* 355 (2017) eaad4998.
- [2] L. Schlapbach, Hydrogen-fuelled vehicles, *Nature* 460 (2009) 809–811.
- [3] D.R. Paudel, U.N. Pan, T.I. Singh, C.C. Gudal, N.H. Kim, J.H. Lee, Fe and P doped 1T-phase enriched WS<sub>2</sub> 3D-dendritic nanostructures for efficient overall water splitting, *Appl. Catal. B: Environ.* 286 (2021), 119897.
- [4] R.W. Coughlin, M. Farooque, Hydrogen production from coal, water and electrons, *Nature* 279 (1979) 301–303.
- [5] L. Wu, L. Yu, F. Zhang, B. McElhenney, D. Luo, A. Karim, S. Chen, Z. Ren, Heterogeneous bimetallic phosphide Ni<sub>2</sub>P-Fe<sub>2</sub>P as an efficient bifunctional catalyst for water/seawater splitting, *Adv. Funct. Mater.* 31 (2020) 2006484.
- [6] F. Zhang, Q. Wang, Redox-mediated water splitting for decoupled H<sub>2</sub> production, *ACS Mater. Lett.* 3 (2021) 641–651.
- [7] Q. Chen, B. Wei, Y. Wei, P. Zhai, W. Liu, X. Gu, Z. Yang, J. Zuo, R. Zhang, Y. Gong, Synergistic effect in ultrafine PtNiP nanowires for highly efficient electrochemical hydrogen evolution in alkaline electrolyte, *Appl. Catal. B: Environ.* 301 (2022), 120754.
- [8] P. Wang, X. Zhang, J. Zhang, S. Wan, S. Guo, G. Lu, J. Yao, X. Huang, Precise tuning in platinum-nickel/nickel sulfide interface nanowires for synergistic hydrogen evolution catalysis, *Nat. Commun.* 8 (2017) 14580.
- [9] L. Liao, S. Wang, J. Xiao, X. Bian, Y. Zhang, M.D. Scanlon, X. Hu, Y. Tang, B. Liu, H. H. Girault, A nanoporous molybdenum carbide nanowire as an electrocatalyst for hydrogen evolution reaction, *Energy Environ. Sci.* 7 (2014) 387–392.
- [10] H. Khan, S.A. Shah, Wu Rehman, F. Chen, CoS<sub>2</sub> nanoparticles-decorated MoS<sub>2</sub>/rGO nanosheets as an efficient electrocatalyst for ultrafast hydrogen evolution, *Adv. Mater. Interfaces* 9 (2022) 2101294.
- [11] W. Xiao, L. Zhang, D. Bukhvalov, Z. Chen, Z. Zou, L. Shang, X. Yang, D. Yan, F. Han, T. Zhang, Hierarchical ultrathin carbon encapsulating transition metal doped MoP electrocatalysts for efficient and pH-universal hydrogen evolution reaction, *Nano Energy* 70 (2020), 104445.
- [12] L. Xiong, B. Wang, H. Cai, H. Hao, J. Li, T. Yang, S. Yang, Understanding the doping effect on hydrogen evolution activity of transition-metal phosphides: modeled with Ni<sub>2</sub>P, *Appl. Catal. B: Environ.* 295 (2021), 120283.
- [13] L. Zhang, Y. Lei, D. Zhou, C. Xiong, Z. Jiang, X. Li, H. Shang, Y. Zhao, W. Chen, B. Zhang, Interfacial engineering of 3D hollow CoSe<sub>2</sub>@ultrathin MoSe<sub>2</sub> core@shell heterostructure for efficient pH-universal hydrogen evolution reaction, *Nano Res.* 15 (2021) 2895–2904.
- [14] P. Yu, F. Wang, T.A. Shifa, X. Zhan, X. Lou, F. Xia, J. He, Earth abundant materials beyond transition metal dichalcogenides: a focus on electrocatalyzing hydrogen evolution reaction, *Nano Energy* 58 (2019) 244–276.
- [15] X. Gan, R. Lv, X. Wang, Z. Zhang, K. Fujisawa, Y. Lei, Z.-H. Huang, M. Terrones, F. Kang, Pyrolytic carbon supported alloying metal dichalcogenides as free-standing electrodes for efficient hydrogen evolution, *Carbon* 132 (2018) 512–519.
- [16] R. Boppella, J. Tan, W. Yang, J. Moon, Homologous CoP/NiCoP heterostructure on N-doped carbon for highly efficient and pH-universal hydrogen evolution electrocatalysis, *Adv. Funct. Mater.* 29 (2018) 1807976.
- [17] W. Xu, G. Fan, S. Zhu, Y. Liang, Z. Cui, Z. Li, H. Jiang, S. Wu, F. Cheng, Electronic structure modulation of nanoporous cobalt phosphide by carbon doping for alkaline hydrogen evolution reaction, *Adv. Funct. Mater.* 31 (2021) 2107333.
- [18] J. Deng, P. Ren, D. Deng, X. Bao, Enhanced electron penetration through an ultrathin graphene layer for highly efficient catalysis of the hydrogen evolution reaction, *Angew. Chem. Int. Ed. Engl.* 54 (2015) 2100–2104.
- [19] Q. Hu, X. Liu, B. Zhu, L. Fan, X. Chai, Q. Zhang, J. Liu, C. He, Z. Lin, Crafting MoC<sub>2</sub>-doped bimetallic alloy nanoparticles encapsulated within N-doped graphene as robust bifunctional electrocatalysts for overall water splitting, *Nano Energy* 50 (2018) 212–219.
- [20] A. Zadick, L. Dubau, N. Sergeant, G. Berthomé, M. Chatenet, Huge instability of Pt/C catalysts in alkaline medium, *ACS Catal.* 5 (2015) 4819–4824.
- [21] Y. Shao-Horn, W.C. Sheng, S. Chen, P.J. Ferreira, E.F. Holby, D. Morgan, Instability of supported platinum nanoparticles in low-temperature fuel cells, *Top. Catal.* 46 (2007) 285–305.
- [22] B. Han, K.A. Stoerzinger, V. Tileli, A.D. Gamalski, E.A. Stach, Y. Shao-Horn, Nanoscale structural oscillations in perovskite oxides induced by oxygen evolution, *Nat. Mater.* 16 (2017) 121–126.
- [23] X. Zhao, H. Ren, L. Luo, Gas bubbles in electrochemical gas evolution reactions, *Langmuir* 35 (2019) 5392–5408.
- [24] Y. Luo, L. Tang, U. Khan, Q. Yu, H.M. Cheng, X. Zou, B. Liu, Morphology and surface chemistry engineering toward pH-universal catalysts for hydrogen evolution at high current density, *Nat. Commun.* 10 (2019) 269.
- [25] M.F. Lagadec, A. Grimaud, Water electrolyzers with closed and open electrochemical systems, *Nat. Mater.* 19 (2020) 1140–1150.
- [26] Z. Zhou, Z. Pei, L. Wei, S. Zhao, X. Jian, Y. Chen, Electrocatalytic hydrogen evolution under neutral pH conditions: current understandings, recent advances, and future prospects, *Energy Environ. Sci.* 13 (2020) 3185–3206.
- [27] H. Yan, Y. Xie, A. Wu, Z. Cai, L. Wang, C. Tian, X. Zhang, H. Fu, Anion-modulated HER and OER activities of 3D Ni-V-based interstitial compound heterojunctions for high-efficiency and stable overall water splitting, *Adv. Mater.* 31 (2019), e1901174.
- [28] C.C. Weng, J.T. Ren, Z.Y. Yuan, Transition metal phosphide-based materials for efficient electrochemical hydrogen evolution: a critical review, *ChemSusChem* 13 (2020) 3357–3375.
- [29] C. Zhang, Y. Luo, J. Tan, Q. Yu, F. Yang, Z. Zhang, L. Yang, H.M. Cheng, B. Liu, High-throughput production of cheap mineral-based two-dimensional electrocatalysts for high-current-density hydrogen evolution, *Nat. Commun.* 11 (2020) 3724.
- [30] Y. Chen, G. Yu, W. Chen, Y. Liu, G.D. Li, P. Zhu, Q. Tao, Q. Li, J. Liu, X. Shen, H. Li, X. Huang, D. Wang, T. Asefa, X. Zou, Highly active, nonprecious electrocatalyst comprising borophene subunits for the hydrogen evolution reaction, *J. Am. Chem. Soc.* 139 (2017) 12370–12373.
- [31] F. Yang, Y. Chen, G. Cheng, S. Chen, W. Luo, Ultrathin nitrogen-doped carbon coated with CoP for efficient hydrogen evolution, *ACS, Catalysis* 7 (2017) 3824–3831.
- [32] J. Li, H. Huang, X. Cao, H.-H. Wu, K. Pan, Q. Zhang, N. Wu, X. Liu, Template-free fabrication of MoP nanoparticles encapsulated in N-doped hollow carbon spheres for efficient alkaline hydrogen evolution, *Chem. Eng. J.* 416 (2021), 127677.
- [33] T. Kim, M. Takahashi, M. Nagai, K. Kobayashi, Preparation and characterization of carbon supported Pt and PtRu alloy catalysts reduced by alcohol for polymer electrolyte fuel cell, *Electrochim. Acta* 50 (2004) 817–821.
- [34] F. Bensebaa, N. Patrito, Y. Le Page, P. L'Ecuyer, D. Wang, Tunable platinum–ruthenium nanoparticle properties using microwave synthesis, *J. Mater. Chem.* 14 (2004) 3378–3384.
- [35] E. Vijayakumar, S. Ramakrishnan, C. Sathiskumar, D.J. Yoo, J. Balamurugan, H. S. Noh, D. Kwon, Y.H. Kim, H. Lee, MOF-derived CoP-nitrogen-doped carbon@NiFeP nanoflakes as an efficient and durable electrocatalyst with multiple catalytically active sites for OER, HER, ORR and rechargeable zinc-air batteries, *Chem. Eng. J.* 428 (2022), 131115.
- [36] Y. Yang, J. Liu, S. Guo, Y. Liu, Z. Kang, A nickel nanoparticle/carbon quantum dot hybrid as an efficient electrocatalyst for hydrogen evolution under alkaline conditions, *J. Mater. Chem. A* 3 (2015) 18598–18604.
- [37] W. Zhong, C. Yang, J. Wu, W. Xu, R. Zhao, H. Xiang, K. Shen, X. Li, Adsorption site engineering: Cu-Ni(OH)<sub>2</sub> sheets for efficient hydrogen evolution, *J. Mater. Chem. A* 9 (2021) 17521–17527.

[38] F. Huang, Z. Liu, Z. Yu, C-alkylation of ketones and related compounds by alcohols: transition-metal-catalyzed dehydrogenation, *Angew. Chem. Int Ed. Engl.* 55 (2016) 862–875.

[39] D. Liu, C. Wang, Y. Yu, B.-H. Zhao, W. Wang, Y. Du, B. Zhang, Understanding the nature of ammonia treatment to synthesize oxygen vacancy-enriched transition metal oxides, *Chem* 5 (2019) 376–389.

[40] Y. Zhu, J. Zhang, Q. Qian, Y. Li, Z. Li, Y. Liu, C. Xiao, G. Zhang, Y. Xie, Dual nanoislands on Ni/C hybrid nanosheet activate superior hydrazine oxidation-assisted high-efficiency H<sub>2</sub> production, *Angew. Chem. Int Ed. Engl.* 61 (2022), e202113082.

[41] D. Ji, L. Fan, L. Tao, Y. Sun, M. Li, G. Yang, T.Q. Tran, S. Ramakrishna, S. Guo, The kirkendall effect for engineering oxygen vacancy of hollow Co<sub>3</sub>O<sub>4</sub> nanoparticles toward high-performance portable zinc-air batteries, *Angew. Chem. Int Ed. Engl.* 58 (2019) 13840–13844.

[42] S. Gao, Z. Sun, W. Liu, X. Jiao, X. Zu, Q. Hu, Y. Sun, T. Yao, W. Zhang, S. Wei, Y. Xie, Atomic layer confined vacancies for atomic-level insights into carbon dioxide electroreduction, *Nat. Commun.* 8 (2017) 14503.

[43] T. Zhang, M.-Y. Wu, D.-Y. Yan, J. Mao, H. Liu, W.-B. Hu, X.-W. Du, T. Ling, S.-Z. Qiao, Engineering oxygen vacancy on NiO nanorod arrays for alkaline hydrogen evolution, *Nano Energy* 43 (2018) 103–109.

[44] Y. Wen, J. Qi, P. Wei, X. Kang, X. Li, Design of Ni<sub>3</sub>N/Co<sub>2</sub>N heterojunctions for boosting electrocatalytic alkaline overall water splitting, *J. Mater. Chem. A* 9 (2021) 10260–10269.

[45] T. Lin, I.-W. Chen, F. Liu, C. Yang, H. Bi, F. Xu, F. Huang, Nitrogen-doped mesoporous carbon of extraordinary capacitance for electrochemical energy storage, *Science* 350 (2015) 1508–1513.

[46] X. Shan, J. Liu, H. Mu, Y. Xiao, B. Mei, W. Liu, G. Lin, Z. Jiang, L. Wen, L. Jiang, An engineered superhydrophilic/superaerophobic electrocatalyst composed of the supported CoMo<sub>x</sub> Chalcogel for overall water splitting, *Angew. Chem. Int Ed. Engl.* 59 (2020) 1659–1665.

[47] P. Zhou, G. Zhai, X. Lv, Y. Liu, Z. Wang, P. Wang, Z. Zheng, H. Cheng, Y. Dai, B. Huang, Boosting the electrocatalytic HER performance of Ni<sub>3</sub>N-V<sub>2</sub>O<sub>3</sub> via the interface coupling effect, *Appl. Catal. B: Environ.* 283 (2021), 119590.

[48] Y.-N. Zhou, F.-L. Wang, J. Nan, B. Dong, H.-Y. Zhao, F.-G. Wang, N. Yu, R.-N. Luan, D.-P. Liu, Y.-M. Chai, High-density ultrafine RuP<sub>2</sub> with strong catalyst-support interaction driven by dual-ligand and tungsten-oxygen sites for hydrogen evolution at 1 A cm<sup>-2</sup>, *Appl. Catal. B: Environ.* 304 (2022), 120917.

[49] N. Yao, P. Li, Z. Zhou, Y. Zhao, G. Cheng, S. Chen, W. Luo, Synergistically tuning water and hydrogen binding abilities over Co<sub>3</sub>N by Cr doping for exceptional alkaline hydrogen evolution electrocatalysis, *Adv. Energy Mater.* 9 (2019) 1902449.

[50] W. Li, H. Zhang, K. Zhang, W. Hu, Z. Cheng, H. Chen, X. Feng, T. Peng, Z. Kou, Monodispersed ruthenium nanoparticles interfacially bonded with defective nitrogen-and-phosphorus-doped carbon nanosheets enable pH-universal hydrogen evolution reaction, *Appl. Catal. B: Environ.* 306 (2022), 121095.